PAPER

Check for updates

HCl post-processing BiOBr photocatalyst: structure, morphology, and composition and their impacts to activity†

Min Hu,[a] Rui Li,[a] Xiaochao Zhang, [ID] *[a] Changming Zhang,[a] Hui Zhang,*[b] Caimei Fan*[a] and Jesse Zhu[b]

This work reports a systematic investigation on the structure, morphology, and composition, and their impacts on photocatalytic performance, for a HCl post-processing BiOBr photocatalyst. We dispersed BiOBr powders into different concentration HCl aqueous solutions to synthesize a series of samples at room temperature. With the HCl concentration increasing, SEM images revealed that as-prepared flower-like BiOBr microspheres transformed gradually into the interweaved nanosheets, and ultimately, obtaining the stacked nanosheet structures. The XRD, EDX, BET, UV-vis DRS and photocurrent data demonstrated that HCl post-processing had in-deep effects on the element composition, specific surface area, optical property and photoelectrochemical properties of samples. Moreover, the detailed formation mechanism and good correlations among their structure, composition, morphology, and enhanced activity have been established by degrading methyl orange (MO) dye molecules under simulated solar light. The HCl post-processing BiOBr samples exhibited better photocatalytic activity and stability than the pure BiOBr sample. Results indicate that there is particular emphasis placed on the roles of H^+ and Cl^- ions in the micro- and macro-performance improvements of BiOBr photocatalysts. Our findings should provide important knowledge for further understanding the roles of H^+ and Cl^- ions in such 'like-BiOX' layered-structure systems.

1. Introduction

Photocatalysis, as one of the most effective and promising methods for wastewater treatment and energy conversion, has garnered growing research interest.[1,2] The main advantage of photocatalytic degradation in dye wastewater is that the non-polluting products are CO_2, H_2O and other inorganic constituents over solar energy and photocatalysts.[3] To exploit efficient and eco-friendly photocatalysts, several studies have focused on the synthesis and research of visible-light-response semiconductor-based materials.[4–6] Recently, bismuth oxyhalides (BiOX, X = Cl, Br, I), with alternative stacking of $[Bi_2O_2]^{2+}$ slabs interleaved by double halogen atom slabs, have become prevalent research topics due to their desirable band gap energies, good optical properties, thermally stimulated conductivities, and excellent photocatalytic abilities.[7–9] More importantly, there exists

a formed internal static electric field between the positive $[Bi_2O_2]^{2+}$ slabs and the negative halogen slabs facilitating the separation and transfer of photo-generated charge carriers, achieving their superior photocatalytic activities.[10–12] However, the shortcoming of stacked [X–Bi–O–Bi–X] layers by small nonbonding (van der Waals) interaction along the *c*-axis will result in the sensitivity of solution acidity or alkalinity and the instability of internal structure.[13,14]

Recent studies found that the acidity or alkalinity of the growth environment could affect the crystal facets, compositions, and morphologies of photocatalysts during the synthesis process.[15–19] For instance, in the synthesis processes of BiOCl using a facile method, it is found that BiOCl, $BiOCl/Bi_2O_2CO_3$ composites and $Bi_2O_2CO_3$ could be successfully prepared by controlling the concentration of NaOH under the same conditions. The superiorities in the structure, morphology and electronic properties made $BiOCl/Bi_2O_2CO_3$ composites possess the higher activity than individual BiOCl and $Bi_2O_2CO_3$ for the degradation of MO under simulated sunlight irradiation.[20] Chang *et al.* synthesized $NaBiO_3/BiOCl$ composite and BiOCl photocatalyst using a novel *in situ* formation approach by regulating the molar ratio of $NaBiO_3$ and HCl aqueous solutions. The $NaBiO_3/BiOCl$ composite showed the higher photocatalytic activity of RhB than pure BiOCl under visible light irradiation because the efficient charge separation on the

[a] College of Chemistry and Chemical Engineering, Taiyuan University of Technology, Taiyuan 030024, PR China. E-mail: zhangxiaochao@tyut.edu.cn; fancm@163.com; Fax: +86-351-6018554

[b] Particle Technology Research Centre, Department of Chemical and Biochemical Engineering, The University of Western Ontario, London, Ontario N6A 5B9, Canada. E-mail: hzhang1@uwo.ca

† Electronic supplementary information (ESI) available. See DOI: 10.1039/c7ra08871j

NaBiO$_3$/BiOCl interface.[21] What's more, Cao *et al.* developed a precipitation transformation method to prepare the microrod Bi$_5$O$_7$I by adding NaOH solution into anomalous smooth plate BiOI precursor suspension, and the higher CB and lower VB positions of Bi$_5$O$_7$I brought about the better photocatalytic activity than BiOI precursor for the degradation on RhB under visible light irradiation.[22] Therefore, to regulate the acidity or alkalinity of the growth environment could not only affect the composition and structural morphology of photocatalyst, but also improve the photocatalytic performance.

Combined with above enlightenment and the intrinsic structural features of BiOX, we explored the effect of HCl post-processing on the compositions, structural morphologies and properties of BiOBr sample by regulating the concentration of HCl solution. The as-prepared samples were characterized by XRD, EDX, SEM, BET and UV-vis DRS. Besides, the photocatalytic activities were evaluated by degrading MO dye molecule under simulated solar light. The formation behaviours of BiOCl$_x$Br$_{1-x}$ solid solutions and BiOCl crystal, as well as their structures, morphologies, specific surface areas, photoelectrochemical properties, band gap energies, and photocatalytic activities were discussed. More importantly, NaCl solution was considered as a substitute of HCl solution under the same experiment conditions to further understand the role of H$^+$ ions compared with HCl solution. We find that H$^+$ ions can accelerate Br$^-$ ions to dissociate from BiOBr lattices. Finally, the possible formation and photocatalytic mechanisms of as-prepared samples are proposed and investigated. It is expected for us to provide the new significant research method for synthesizing a series of such Bi-based layer-structure photocatalytic materials.

2.   Experimental

2.1   Raw materials and synthesis of samples

Bismuth nitrate pentahydrate (Bi(NO$_3$)$_3$·5H$_2$O) and potassium bromide (KBr) were purchased from Tianjin Sinopharm Chemical Reagent (Co. Ltd.) and Tianjin Zhiyuan Reagent (Co. Ltd.) respectively. Ethylene glycol and Anhydrous ethanol were provided by Tianjin Kemiou Chemical Reagent (Co. Ltd.) and Tianjin Guangfu Chemical Reagent (Co. Ltd.), respectively. HCl was obtained from Tianjin Medical Company. All the reagents belong to the analytic purity. Deionized water was used throughout this work.

In a typical procedure, 0.02 mol Bi(NO$_3$)$_3$·5H$_2$O was dissolved in 80 mL EG solution at room temperature with continuous stirring until the solution became transparent. Subsequently, 0.02 mol KBr was poured into the previous solution for 1 h. After adding 40 mL H$_2$O into the mixture solution for 4 h with continuous stirring, the white precipitates were filtrated and washed successively with deionized water and ethanol, then dried at 60 °C for 12 h. The obtained sample was denoted as BOB.

1.00 g BOB powders were dispersed in X mL (X = 0.25, 0.50, 0.75, 1.00, 1.25) HCl solutions with 40 mL H$_2$O for 1 h at room temperature with continuous stirring. The white precipitates were collected, washed with deionized water and ethanol several times, then dried at 60 °C overnight. The as-prepared samples

were obtained and denoted as BOB-HC1, BOB-HC2, BOB-HC3, BOB-HC4, and BOB-HC5.

2.2   Characterization

The crystal structures of as-prepared samples were measured by X-ray diffraction (XRD) (DX-2700 diffractometer, Japan) with Cu Kα radiation and a scanning rate of 8° min^{-1} in the range from 10° to 80°. The morphologies and chemical compositions were observed on a Nanosem 430 (FEI, America) field emission scanning electron microscopy at an operating voltage of 10 kV, with an energy dispersive X-ray (EDX) microanalysis system. The specific surface area and porous structures were determined by nitrogen adsorption and desorption and using the V-Sorb 4800P analyzer. The photocurrent was measured with a CHI660D electrochemistry workstation using a three-electrode system. The UV-vis diffuse reflectance spectra (DRS) were acquired on a UV-vis spectrophotometer (UV-3600, Shimadzu, Japan).

2.3   Photocatalytic test

The photocatalytic activities of all the as-prepared samples were measured from degradation of MO dye under simulated solar light irradiation. Experiments were carried out in a 100 mL beaker at room temperature in air, 0.10 g sample was dispersed in 100 mL MO solution (10 mg L^{-1}) and stirred magnetically for 20 min in the dark to reach adsorption–desorption equilibrium. The reactor was then irradiated by a 500 W Xe lamp as the simulated solar light source. During irradiation times, 3 mL of suspension was taken from the reaction cell at irradiation time intervals of 10 min. The concentration of MO solution was analyzed by a Varian Cary-50 UV-vis spectrophotometer. The degradation efficiency (D) of MO was calculated by the following formula:

$$D = (1 - c_t/c_0) \times 100\%$$

where c_0 is the initial concentration of MO and c_t is the concentration of MO after irradiation for a time period of t (min).

3.   Results and discussion

3.1   Structure and composition

To identify the influence of different concentration HCl solutions post-processing on the structure and composition of BiOBr photocatalyst, XRD measurement was performed, as shown in Fig. 1. It is found that the XRD patterns of all the as-prepared samples have the similar diffraction peaks, demonstrating that there exist the isostructural compounds and no separated phase. All the diffraction peaks of as-prepared BOB sample are readily indexed to tetragonal phase BiOBr (JCPDS card no. 78-0348).[23] With the HCl concentration increasing, the main strong peaks corresponding to {001}, {002}, {101}, {112} crystal planes of BOB-HC1, BOB-HC2, BOB-HC3 and BOB-HC4 gradually shift to the larger angles compared with BOB sample, indicating the formation behaviour of solid solution.[24–27] Besides, the XRD pattern of BOB-HC5 sample is
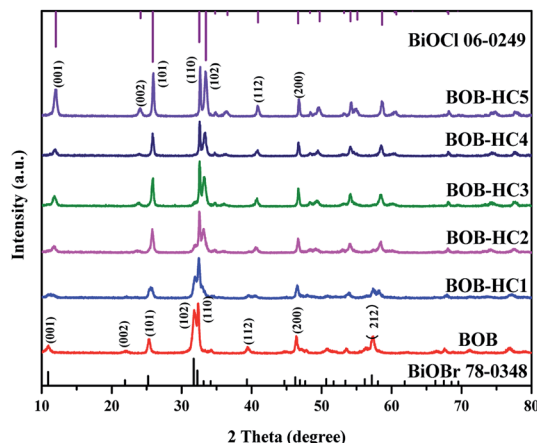
Fig. 1 XRD patterns of as-prepared samples *via* different concentration HCl solutions post-processing BiOBr.

indexed to tetragonal phase BiOCl (JCPDS card no. 06-0249),[28] indicating the formation of BiOCl crystal. Therefore, with the HCl concentration increasing, more and more Cl$^-$ ions react with BiOBr, and BiOBr sample gradually transforms into BiOCl$_x$Br$_{1-x}$ solid solutions and ultimately turns into BiOCl. The results reveal that HCl post-processing plays a vital role in composition and structure changes of BiOBr.

In order to further clarify the chemical composition of as-prepared samples, the typical EDX of BOB, BOB-HC2, BOB-HC3 and BOB-HC5 samples was carried out. As shown in Fig. S1,† the peaks near 1.50 keV and 2.65 keV correspond to the Br and Cl elements, respectively. With the HCl concentration increasing, the content of Br element gradually decreases and that of Cl element gradually increases. A detailed analysis of the element composition and distribution of BOB-HC3 sample by elemental mapping was shown in Fig. 2. It should be noted that Bi, O, Cl and Br elements revealed the uniform distribution feature, indicating the formation of BiOCl$_x$Br$_{1-x}$ solid solution rather than a heterostructure composite of BiOBr and BiOCl. The result is good agreement with XRD analysis, further confirming that HCl post-processing BiOBr should affect the composition and distribution of as-prepared samples.
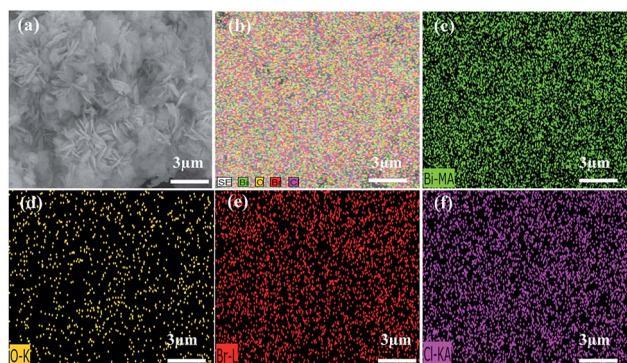
3.2 Morphology and formation mechanism

Fig. 3 gives the SEM images of as-prepared BOB, BOB-HC2, BOB-HC3, and BOB-HC5 samples. The BOB sample presents the hierarchical flower-like microspheres assembled by nanosheets with a high yield and the approximated diameter of single BOB microsphere structure ranges from 0.8–1.0 μm (Fig. 3a and b). Compared with BOB sample, the morphologies of BOB-HC2 and BOB-HC3 samples have the notable variations. The flower-like microspheres are destroyed and the nanosheets loosely interweaved, leaving an obvious space between inter-sheet voids (Fig. 3c–f). For BOB-HC5 sample, we could hardly see the whole flower-like microspheres and many inhomogeneous nanoplates are closely stacked together (Fig. 3g and h). Thus, HCl post-processing BiOBr affects the structural morphologies of as-prepared samples.

The changes of structure, composition, and morphology could be described as a recrystallization process, as shown in Fig. 4. BiOBr photocatalyst synthesized by hydrolysis method is inclined to the flower-like microspheres because the viscosity of EG solvent and the minimization of total surface energy in Ostwald ripening process will lead to the growth of nanosheets in the direction of bending and formation of hierarchical flowerlike structures.[29,30] When BiOBr powders are dispersed into different concentration HCl solutions, the BiOBr microspheres are

Fig. 2 EDX mappings of (a and b) BOB-HC3, (c) Bi, (d) O, (e) Br, and (f) Cl.
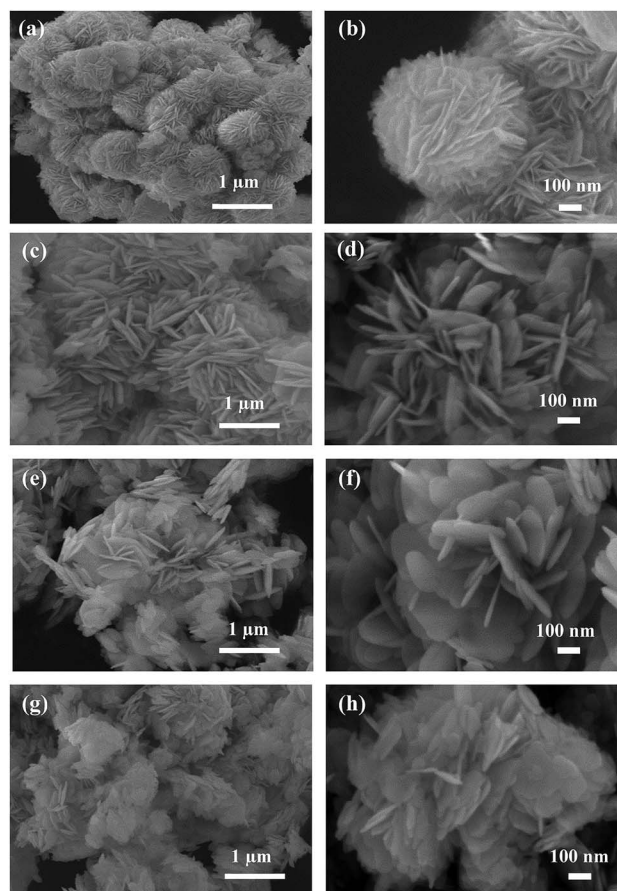

Fig. 3 SEM images of (a and b) BOB, (c and d) BOB-HC2, (e and f) BOB-HC3, and (g and h) BOB-HC5 samples.
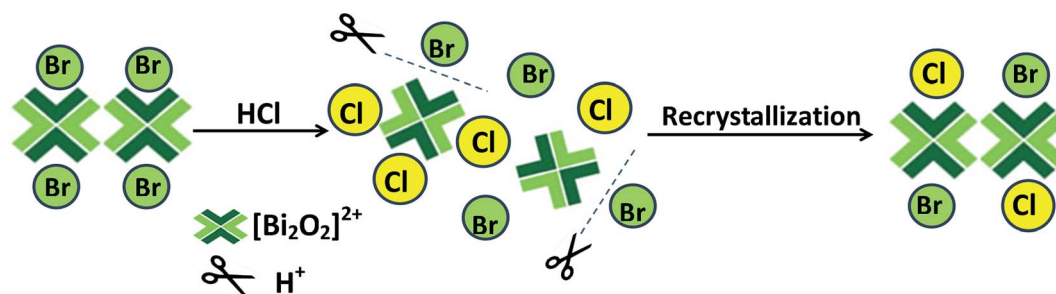
Fig. 4   The possible formation mechanism of BiOCl$_x$Br$_{1-x}$ samples.

destroyed quickly under the strong acid environment because the corrosive effects of H$^+$ ions make Br$^-$ ions dissociate from BiOBr lattice, and the [Bi$_2$O$_2$]$^{2+}$ ions and Br$^-$ ions dissolve into solution, which will be further discussed in later section about the effect of H$^+$ ions of HCl. Moreover, the solubility product constant (K_{sp}) of BiOCl (1.8 × 10^{-31}, 298.15 K) is much smaller than that of BiOBr (3.0 × 10^{-7}, 298.15 K),[31,32] so that BiOBr crystal could adopt a thermodynamically favored direction to transform into BiOCl crystal. Thus, [Bi$_2$O$_2$]$^{2+}$ ions would immediately react with Cl$^-$ and Br$^-$ ions to form BiOCl$_x$Br$_{1-x}$ solid solution. With the HCl concentration increasing in the reaction process, more and more Cl$^-$ ions react with [Bi$_2$O$_2$]$^{2+}$ ions, resulting in the formation of BiOCl crystal (in Fig. 4). As can be seen from the SEM images of as-prepared samples, the flower-like microspheres of BiOBr transform gradually into the interweaved nanosheets, and ultimately turn into the closely stacked nanosheets to decrease the total surface energy of crystal. What's more, the morphologies of BiOCl$_x$Br$_{1-x}$ solid solutions and BiOCl crystal were affected by the small viscosity of water solvent and nanosheets anisotropic growth.[33]

3.3   Surface area analysis

The variation in the structural morphology of photocatalyst could bring about the different specific surface areas and porous structures, which will play an important role in the photocatalytic performance. The surface areas and porous structures of samples were obtained based on nitrogen adsorption and desorption (in Fig. S2†). The isotherms of BOB, BOB-HC2, BOB-HC3 and BOB-HC5 samples corresponded to type IV with H3 hysteresis loop, indicating their mesoporous materials.[34,35] Besides, the pore size distribution of sample was measured using the Barrett–Joyner–Halenda (BJH) method from nitrogen adsorption–desorption isotherm. The formation of mesopores could be explained to the interspaces caused from intercrossed nanosheets. The BET surface areas (in Table 1) of as-prepared samples increase gradually, and reach the

maximum of BOB-HC2 sample, then decrease with the HCl concentration increasing. The change trend is in good agreement with the morphology variation feature, where the flower-like microspheres of samples become interweaved nanosheets gradually, and ultimately turn into closely stacked nanosheets with the HCl concentration increasing. Thus, the composition changes of as-prepared samples will lead to the various morphologies through regulating the concentration HCl solutions, which further affects their surface areas or pore structures. However, the variations in specific surface areas and porous structures were too small to affect the adsorption for MO, thus the change of BET surface areas was not the key factor for enhanced photocatalytic performance.

3.4   Optical absorption property

The UV-vis diffuse reflectance spectra (in Fig. 5) of all as-prepared samples were provided for further verifying the experimental results that BiOBr samples could turn into the BiOCl$_x$Br$_{1-x}$ solid solutions and BiOCl samples via different concentration HCl solutions post-processing BiOBr samples on the basis of the different optical absorption properties. With the HCl concentration increasing, it is obviously found that the optical absorption edges of as-prepared samples shift monotonically to the shorter wavelength, indicating that there is indeed the formation of BiOCl$_x$Br$_{1-x}$ solid solution.[36] Moreover, the band gap energy (E_g), conduction band (CB) and valence band (VB) positions of as-prepared samples can be calculated from diffused reflectance spectra to understand the changes in band structures of as-prepared samples caused by their different compositions. The band gap (E_g) of each sample is estimated using equation $E_g = 1239/\lambda_g$,[3] where λ_g is the band gap wavelength. Based on DRS results, the estimated band gaps energy (in Table 2) ranges from 2.79 to 3.14 eV with the HCl concentration increasing.

As well-known from the theory calculations, BiOBr, BiOCl$_x$-Br$_{1-x}$ solid solutions, and BiOCl with similar structures have

Table 1   BET specific surface area (S_{BET}) and pore parameters of as-prepared samples

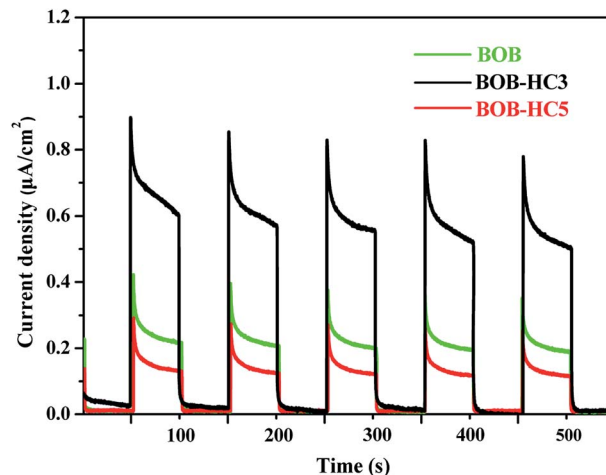| Samples	BOB	BOB-HC1	BOB-HC2	BOB-HC3	BOB-HC4	BOB-HC5
S_{BET} (m^2 g^{-1})	20.123	21.984	24.092	17.669	15.016	14.119
Pore size (nm)	20.563	33.584	27.109	19.887	25.870	27.451

Fig. 5   UV-vis diffuse reflectance spectra of as-prepared samples.

Fig. 6   Photocurrent responses of BOB, BOB-HC3 and BOB-HC5 samples measured in 1 M Na_2SO_4 solutions under Xe-lamp irradiation.

different electronic properties due to the existence of difference halogen atoms. The conduction band minimum (CBM) of $BiOCl_xBr_{1-x}$ compound is composed of Bi 6p states and the valence band maximum (VBM) consists of Bi 6s, O 2p, Cl 3p and Br 4p states.[37] The redox abilities of compounds depend on the potential of CB and VB. The XRD, EDX and DRS data indicate that HCl post-processing has an important effect on the compositions of BiOBr samples, so that BOB-HC1, BOB-HC2, BOB-HC3, BOB-HC4 and BOB-HC5 samples will exhibit the different CB and VB edge positions and photocatalytic activities compared with BOB samples. The VB and CB edge positions of as-prepared samples can be calculated through the following equations:[38]

$$E_{CB} = \chi - E_C - 0.5E_g$$

$$E_{VB} = E_{CB} + E_g$$

where χ is the electronegativity of semiconductor, E_C is the energy of free electrons on the hydrogen scale (about 4.5 eV). The relative electronegativity of atoms is listed in Table S1.† The calculated VB and CB edge positions for as-prepared samples are listed in Table 2. It can be seen that CB edge positions of as-prepared samples have no significant change. However, the VB edge positions increase from 3.07 to 3.43 V, meaning that the oxidation ability should become stronger with the HCl concentration increasing.

3.5   Photoelectrochemical properties

As we widely known that the separation efficiency of electrons and holes is a key factor for photocatalytic reaction. Fig. 6 shows the transient photocurrent responses of BOB, BOB-HC3 and BOB-HC5 samples under intermittent Xe lamp irradiation. In general, the higher photocurrent intensity means the better separation efficiency of electrons and holes.[39] As can be seen, the photocurrent density is low in dark, then the photocurrent density rapidly increased after that the lamp is turned on. Compared with BOB sample, the BOB-HC3 solid solution exhibits a noticeable enhanced photocurrent density, which is about two times than that of BOB. While BOB-HC5 sample shows the weaker photocurrent density than BOB. Thus, the most enhanced photocurrent density of BOB-HC3 solid solution reveals the greatest inhabitation of the recombination of photoinduced electrons and holes. Moreover, the results indicate HCl post-processing BiOBr should play a vital role in the enhanced separation efficiency of photoinduced electrons and holes.

3.6   Photocatalytic activity and stability

The photocatalytic activities of as-prepared samples were evaluated by the degradation of MO dye under simulated solar light irradiation, as shown in Fig. 7a. It can be clearly found that BOB and BOB-HC5 samples show the poor photocatalytic activities for the degradation on MO with the percentages of 63.24% and 43.49% after 40 min, respectively. Whereas, the BOB-HC1, BOB-HC2, BOB-HC3 and BOB-HC4 solid solutions exhibit the better photocatalytic activities than BOB and BOB-HC5 samples. Among them, the BOB-HC3 sample displays the best activity and the maximum removal efficiency of 93.9% for 30 min. With the time increasing from 30 min to 40 min, the photocatalytic MO degradation efficiency increases up to 98.77%. Moreover, the recycling experiments (in Fig. 7b) indicate that the removal efficiency of BOB-HC3 sample still maintains about 93.50% after four-time recycling runs. Moreover, compared with fresh

Table 2   Physicochemical properties of as-prepared samples calculated from diffuse reflectance spectra

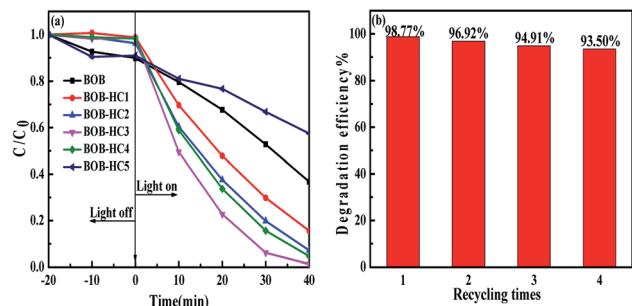| Samples	χ (eV)	E_g (eV)	E_{CB} (V)	E_{VB} (V)
BOB	6.17	2.79	0.28	3.07
BOB-HC1	6.21	2.85	0.29	3.14
BOB-HC2	6.25	2.92	0.29	3.21
BOB-HC3	6.28	2.97	0.30	3.27
BOB-HC4	6.32	3.09	0.30	3.39
BOB-HC5	6.36	3.14	0.30	3.43

Fig. 7 (a) Photocatalytic degradation efficiencies of MO under simulated solar light irradiation with as-prepared samples, (b) recycling test of photocatalytic degradation over BOB-HC3 sample.

BOB-HC3 sample (in Fig. S3a†), the structural morphology of BOB-HC3 sample after recycle has no obvious change (in Fig. S3b†). The results reveal that the BOB-HC3 sample has highly stable photocatalytic performance.

3.7 Active species and photocatalytic mechanism of BOB-HC3 sample

Fig. 8 displays the effect of active species scavengers on the photocatalytic degradation of MO over BOB-HC3 sample. The scavengers of isopropanol (IPA) and sodium formate (SF) are added to the reaction system to examine the roles of reactive species hydroxyl radicals ($\cdot$OH) and holes (h^+), respectively. The addition of IPA has a slight effect on the photocatalytic degradation MO efficiency, implying that $\cdot$OH should be not the key active oxidative species. However, the addition of SF causes an obvious decrease of MO degradation efficiency, confirming the main active species of h^+. To understand the role of superoxide radical ($\cdot O_2^-$), N_2 purging experiment was performed, and the photocatalytic degradation efficiency on MO is suppressed. Hence, $\cdot O_2^-$ plays a significant role in such photocatalytic process. Therefore, h^+ and $\cdot O_2^-$ should be the main active species for photocatalytic degradation on MO over BOB-HC3
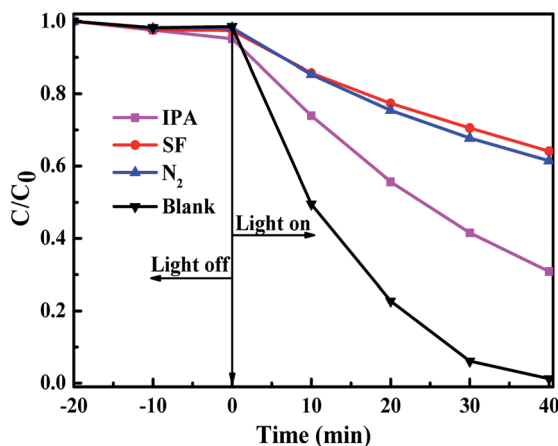

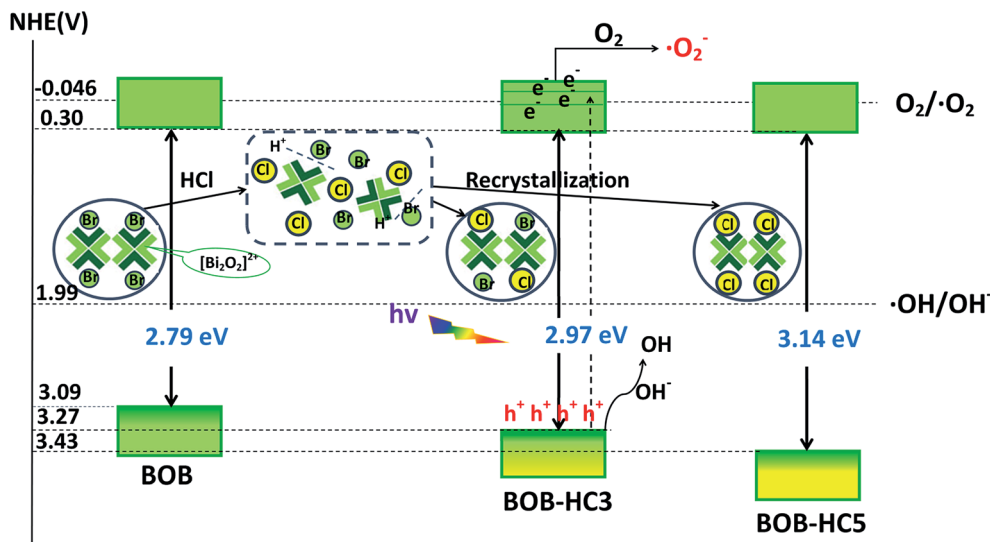Fig. 8 Photocatalytic degradation efficiencies of MO over BOB-HC3 with different scavengers.

catalyst, achieving the efficient separation of photo-induced electron–hole pairs.

The higher photocatalytic activities of $BiOCl_xBr_{1-x}$ solid solutions than BiOBr and BiOCl samples on the degradation of MO dye under simulated solar light irradiation are discussed and summarized, as followings: (1) the as-prepared samples with different compositions have different E_g values, VB and CB edge positions (as seen in Scheme 1). The E_g values increased with the HCl content increasing, confirming the lower utilization efficiency of energy.[40] The trapping experiments results show that the photoinduced electrons from the higher conduction band could be captured by surface-absorbed oxygen to form superoxide radical ($\cdot O_2^-$), which would contribute to achieve the improvement of photocatalytic activity. What's more, there is no any obvious variation of CB edge positions, indicating the existence of similar reducing ability. Furthermore, the more positive VB edge potentials (as seen in Table 2) of as-treated BiOBr with a higher concentration of HCl demonstrates the stronger oxidation ability. Thus, the holes (h^+) in VB of photocatalyst could react with OH^-/H_2O to form $\cdot$OH or directly react with organic molecules to resolve into the smaller organic molecules.[41] The competition between the utilization efficiency of energy and the oxidation ability for as-prepared samples may be a key factor for enhanced photocatalytic activity of $BiOCl_xBr_{1-x}$ solid solution. (2) The analysis results of transient photocurrent responses of as-prepared samples reveal that the photocurrent density of BOB-HC3 solid solution was about two times than BOB, confirming the enhanced separation efficiencies of photogenerated carriers through proper concentration HCl solution post-processing BiOBr. Therefore, mutual competition between these factors may achieve the highest photocatalytic activities of BOB-HC3 among the as-prepared samples.

3.8 Effect of H^+ ions on the formation behaviors of as-prepared samples

To further confirm the effect of H^+ ions of HCl solution on the composition and morphology of BiOBr samples in the reaction system, 0.88 g NaCl solution is used to replace 1.25 mL HCl solution under the same conditions. The precipitate is collected and regarded as BOB-NC. Finally, the BOB-NC sample is characterized by XRD and SEM. All the diffraction peaks of BOB-NC sample can be indexed to tetragonal phase BiOBr (JCPDS card no. 78-0348), and the intensity of diffraction peaks of BOB-NC sample is almost the same as that of BOB sample (in Fig. 9). Compared with SEM images of BOB-NC (in Fig. S4a†) and BOB samples (in Fig. S4b†), the morphologies of BOB-NC sample still maintain the structure of flower-like microspheres, and the average diameter of single microsphere is about 0.8–1.0 μm. The results indicate that NaCl post-processing BiOBr has no significant influence on the structure, composition and morphology of BiOBr sample. However, HCl post-processing plays an in-deep role in the element composition, morphology and photocatalytic activity on BiOBr sample. Obviously, the existence of H^+ ions in HCl solution could lead to the effective separation of Br^- ions and $[Bi_2O_2]^{2+}$ ions, helping to achieve the subsequent reactions among Cl^- ions, Br^- ions and $[Bi_2O_2]^{2+}$ ions.

Scheme 1 The possible formation processes of BOB-HC3 and BOB-HC5 samples, and photocatalytic mechanism of BOB-HC3.
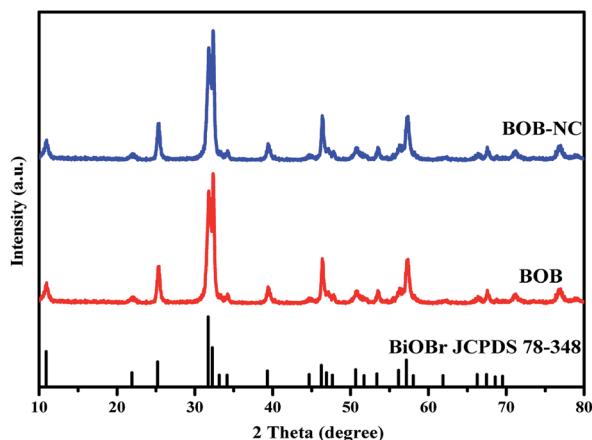

Fig. 9 XRD patterns of BOB-NC and BOB samples.

4. Conclusions

In summary, we dispersed BiOBr powders into different concentration HCl solutions to synthesize $BiOCl_xBr_{1-x}$ solid solution and BiOCl sample. Compared with pure BiOBr, as-prepared $BiOCl_xBr_{1-x}$ solid solution and BiOCl sample possess the similar structures and different compositions. The changes of structure and composition could induce the variations of the morphology, surface area, band gaps energy, and other properties, further affect the photocatalytic performance. The BOB-HC3 solid solution displays the highest photocatalytic removal efficiency of MO dye that reaches 98.77% after 40 min under simulated solar light, higher than 35.53% over pure BiOBr sample. After the 4th recycling test, the photocatalytic removal efficiency of MO dye still maintains about 93.50%, indicating the more favorable photocatalytic stability. The enhanced photocatalytic performance of BOB-HC3 sample is closely related to the suitable band-gap structure and better

separation efficiency of electrons and holes. Moreover, the corrosive effect of H$^+$ ions of HCl ruptures the original layered structure of BiOBr, resulting in that Cl$^-$ ions react with $[Bi_2O_2]^{2+}$ and Br$^-$ ions to form the $BiOCl_xBr_{1-x}$ solid solution. Our findings should provide a new idea and method to synthesize efficient photocatalysts based on the sensitivity of BiOBr to the acidity of growth environment and the solubility product constant (K_{sp}) of other photocatalysts with such BiOBr-layer structures.

Conflicts of interest

There are no conflicts to declare.

Acknowledgements

Notes and references

1 S. Malato, P. Fernández-Ibáñez, M. I. Maldonado, J. Blanco and W. Gernjak, *Catal. Today*, 2009, **147**, 1–59.
2 V. P. Indrakanti, J. D. Kubicki and H. H. Schobert, *Energy Environ. Sci.*, 2009, **2**, 745–758.
3 S. Shenawi-Khalil, V. Uvarov, S. Fronton, I. Popov and Y. Sasson, *Appl. Catal., B*, 2012, **117**, 148–155.
4 H. L. Lin, X. Li, J. Cao, S. F. Chen and Y. Chen, *Catal. Commun.*, 2014, **49**, 87–91.
5 Y. Liu, X. Z. Yuan, H. Wang, X. H. Chen, S. S. Gu, Q. Jiang, Z. B. Wu, L. B. Jiang and G. M. Zeng, *RSC Adv.*, 2015, **5**, 33696–33704.

6 W. N. Wang, W. J. An, B. Ramalingam, S. Mukherjee, D. M. Niedzwiedzki, S. Gangopadhyay and P. Biswas, *J. Am. Chem. Soc.*, 2012, **134**, 11276–11281.

7 H. J. Zhang, L. Liu and Z. Zhou, *RSC Adv.*, 2012, **2**, 9224–9229.

8 X. Xiao, C. Liu, R. P. Hu, X. X. Zuo, J. M. Nan, L. S. Li and L. S. Wang, *J. Mater. Chem.*, 2012, **22**, 22840–22843.

9 H. B. Yin, X. F. Chen, R. J. Hou, H. J. Zhu, S. Q. Li, Y. N. Huo and H. X. Li, *ACS Appl. Mater. Interfaces*, 2015, **7**, 20076–20082.

10 H. F. Cheng, B. B. Huang and Y. Dai, *Nanoscale*, 2014, **6**, 2009–2026.

11 Q. Q. Du, W. P. Wang, Y. Z. Wu, G. Zhao, F. K. Ma and X. P. Hao, *RSC Adv.*, 2015, **5**, 31057–31063.

12 Y. Y. Li, H. C. Yao, J. S. Wang, N. Wang and Z. J. Li, *Mater. Res. Bull.*, 2011, **46**, 292–296.

13 G. Chen, G. L. Fang and G. D. Tang, *Mater. Res. Bull.*, 2013, **48**, 1256–1261.

14 J. Li, Y. Yu and L. Z. Zhang, *Nanoscale*, 2014, **6**, 8473–8488.

15 J. Jiang, K. Zhao, X. Y. Xiao and L. Z. Zhang, *J. Am. Chem. Soc.*, 2012, **134**, 4473–4476.

16 C. S. Lim, J. H. Ryu, D. H. Kim, S. Y. Cho and W. C. Oh, *J. Ceram. Process Res.*, 2010, **11**, 736–741.

17 Y. Lu, Y. Zhao, J. Z. Zhao, Y. Song, Z. F. Huang, F. F. Gao, N. Li and Y. W. Li, *Cryst. Growth Des.*, 2015, **15**, 1031–1042.

18 J. L. Wang, Y. Yu and L. Zhang, *Appl. Catal., B*, 2013, **136**, 112–121.

19 H. P. Li, T. X. Hu, J. Q. Liu, S. Song, N. Du, R. J. Zhang and W. G. Hou, *Appl. Catal., B*, 2016, **182**, 431–438.

20 X. C. Zhang, T. Y. Guo, X. W. Wang, Y. W. Wang, C. M. Fan and H. Zhang, *Appl. Catal., B*, 2014, **150**, 486–495.

21 X. F. Chang, G. Yu, J. Huang, Z. Li, S. F. Zhu, P. F. Yu, C. Cheng, S. B. Deng and G. B. Ji, *Catal. Today*, 2010, **153**, 193–199.

22 J. Cao, X. Li, H. L. Lin, B. V. Xu, B. D. Luo and S. F. Chen, *Mater. Lett.*, 2012, **76**, 181–183.

23 N. N. Guo, Y. L. Cao, Y. L. Rong and D. Z. Jia, *RSC Adv.*, 2016, **6**, 106046–106053.

24 X. Zhang, L. W. Wang, C. Y. Wang, W. K. Wang, Y. L. Chen, Y. X. Huang, W. W. Li, Y. J. Feng and H. Q. Yu, *Chem.–Eur. J.*, 2015, **21**, 11872–11877.

25 Y. Y. Liu, W. J. Son, J. B. Lu, B. B. Huang, Y. Dai and M. H. Whangbo, *Chem.–Eur. J.*, 2011, **17**, 9342–9349.

26 H. Gnayem and Y. Sasson, *ACS Catal.*, 2013, **3**, 186–191.

27 K. X. Ren, J. Liu, J. Liang, K. Zhang, X. Zheng, H. D. Luo, Y. B. Huang, P. J. Liu and X. B. Yu, *Dalton Trans.*, 2013, **42**, 9706–9712.

28 X. N. Wang, H. C. Chen, H. J. Li, G. Mailhot and W. B. Dong, *J. Colloid Interface Sci.*, 2016, **478**, 1–10.

29 Z. S. Liu, B. T. Wu, D. H. Xiang and Y. B. Zhu, *Mater. Res. Bull.*, 2012, **47**, 3753–3757.

30 J. Zhang, F. J. Shi, J. Lin, D. F. Chen, J. M. Gao, Z. X. Huang, X. X. Ding and C. C. Tang, *Chem. Mater.*, 2008, **20**, 2937–2941.

31 L. W. Shan, G. L. Wang, L. Z. Liu and Z. Wu, *J. Mol. Catal. A: Chem.*, 2015, **406**, 145–151.

32 C. H. Deng and H. M. Guan, *Mater. Lett.*, 2013, **107**, 119–122.

33 R. Li, X. Y. Gao, C. M. Fan, X. C. Zhang, Y. W. Wang and Y. F. Wang, *Appl. Surf. Sci.*, 2015, **355**, 1075–1082.

34 Y. H. Ao, H. Tang, P. F. Wang, C. Wang, J. Hou and J. Qian, *Composites, Part B*, 2014, **59**, 96–100.

35 X. Y. Gao, X. C. Zhang, Y. W. Wang, S. Q. Peng, B. Yue and C. M. Fan, *Chem. Eng. J.*, 2015, **263**, 419–426.

36 S. Shenawi-Khalil, V. Uvarov, Y. Kritsman, E. Menes, I. Popov and Y. Sasson, *Catal. Commun.*, 2011, **12**, 1136–1141.

37 H. J. Zhang, L. Liu and Z. Zhou, *Phys. Chem. Chem. Phys.*, 2012, **14**, 1286–1292.

38 C. Q. Wen, Z. Y. Fan and X. C. Song, *Ceram. Int.*, 2016, **42**, 14533–14542.

39 J. Xie, Y. L. Cao, D. Z. Jia and Y. Z. Li, *J. Colloid Interface Sci.*, 2017, **503**, 115–123.

40 X. M. Mao and C. M. Fan, *Int. J. Miner., Metall. Mater.*, 2013, **20**, 1089–1096.

41 X. C. Zhang, B. Q. Lu, R. Li, X. L. Li, X. Y. Gao and C. M. Fan, *Sep. Purif. Technol.*, 2015, **154**, 68–75.